Bias dependent admittance spectroscopy of thin film solar cells: KF post deposition treatment, accelerated lifetime testing, and their effect on the CVf loss maps.

Thierry Kohl[1,2,3,*], Guy Brammertz[1,2,3], Jessica de Wild[1,2,3], Dilara Gokcen Buldu[1,2,3], Gizem Birant[1,2,3], Marc Meuris[1,2,3], Jozef Poortmans[1,2,3,4,5], Bart Vermang[1,2,3]

[1] Institute for Material Research (IMO), Hasselt University (partner in Solliance), Wetenschapspark 1, 3590 Diepenbeek, Belgium

[2] Imec division IMOMEC (partner in Solliance), Wetenschapspark 1, 3590 Diepenbeek, Belgium

[3] EnergyVille, Thorpark, Poort Genk 8310 & 8320, 3600, Belgium

[4] imec (partner in Solliance), Kapeldreef 75, Leuven, 3001, Belgium

[5] Department of Electrical Engineering, KU Leuven, Kasteelpark Arenberg 10, 3001 Heverlee, Belgium

**Corresponding author.*

Email address: thierry.kohl@imec.be

***Abstract*— Modern solar cell designs include an always larger variety of elements and additional layers. This approach is usually successful and leads to the development of increasingly efficient materials. However, scientifically, it makes the drawing of accurate conclusions always more challenging, due to the growing number of elements, possible defects, interfaces, and barriers. To try and remedy this problem, we developed a novel way to investigate solar cells by representing bias dependent admittance spectroscopy (CVf) measurement data in the form of a 2D loss map. In this contribution, we elaborate how this technique can be used experimentally, present some concrete results we obtained from measurements on ultra-thin CIGS solar cells and explain how they can be interpreted. We identify 3 major response domains on our typical CVf loss maps. One at high frequency that covers most of the bias range and can be related to series resistance. One at low frequency, mostly visible at strong positive and negative biases, which is related to shunt and dissipation. The last response domain, close to 100kHz and impacting most of the bias range, can be identified as a defect response of the material. Using CVf measurements on samples with KF post deposition treatment, known for its grain boundary passivation properties, and samples that were previously submitted to accelerated lifetime testing in damp heat conditions, the impact of bulk defects, grain boundaries and conduction band offsets are investigated.**

***Index Terms* — admittance spectroscopy, thin film photovoltaics, CIGS, loss map, post deposition treatment, alkali doping.**

In the race for the renewable energy source of the future, $Cu(In,Ga)Se_2$ (CIGS) is one of the more promising candidates among the thin film photovoltaic technologies, as efficiencies upward of 23% have already been achieved [1]. These high efficiencies only become possible by applying varying types of treatments to the material and by optimizing every single layer and interface that make up the full solar cell stack. Various alkali treatments of the absorber [2–10], and alternative buffer or window layers [11–14] are all commonly used techniques to optimize the power conversion efficiency of CIGS solar cells.

The problem that might have to be faced when all of these or other novel techniques are implemented into the architecture is that the addition of new elements and layers might have unforeseen detrimental consequences on the workings of the devices. Indeed, the addition of new elements can lead to the creation of new, previously unobserved defects and phases in the materials. The addition of new layers, on the other hand, leads to the creation of new interfaces that might not be optimal. If the research community wants to be able to eventually understand, explain and potentially correct these new problems, we need to come up with novel solutions to study them as well as new ways to extract the data from the measurement methods that are already available to us.

One such method is admittance spectroscopy as it is a thoroughly discussed and commonly used technique to study both MOS and pn-junctions effectively [15–17]. Moreover, it has been used quite extensively to study thin film solar cells of all types already, and CIGS in particular [16,18–23]. In a typical admittance measurement, the evolution of the admittance response of the material as a function of temperature would be investigated [16,17,24–26]. Alternatively, information can be extracted from the change in admittance when the solar cell is submitted to various bias potentials as well [19,24,25,27]. In our previous contribution to the topic [28], we developed and discussed the possibility of measuring the admittance as a combined function of frequency and bias potential. The data set that is obtained following one such measurement is understandably very large. Analyzing every traditional plot separately is a long and arduous task.

To simplify it we proposed to represent the derivative of the capacitance as a function of the frequency over the whole bias and frequency range. This gives rise to a two-dimensional contour map as it can be seen in figure 1. This type of representation is highly visual and makes the analysis of this large amount of data much more intuitive and straightforward. These maps were dubbed "CVf Loss Map" since every one of the high intensity spots, or response domains, on this visual representation can be identified as being one or another type of imperfection in the functioning of the solar cell. These imperfections can in turn be linked to a loss in its overall performance [28]. Using SCAPS simulations [29], we were able to show that specific types of losses could be explained either by effects related to the measurement itself, or specific types of defects and barriers in the solar cell. For various types of defects, barriers, and resistances, we were able to draw some early conclusions as to the probable origin of some of the features on the plotted CVf loss maps. Indeed, by carefully selecting our defect energies and types, we were able to simulate a loss map very similar to the one we obtained through experimental measurement.

In the present contribution, we will go into further detail concerning the experimental part of our approach. Using the knowledge we acquired from the simulations, we can identify some of the more common features on the measured maps and determine their respective origin. We analyzed CIGS solar cells that underwent specific treatments. By using our newly developed representation method, as well as our previous simulation results, we determined what impact these production steps had on the CVf loss map [28].

1. EXPERIMENTAL METHODS

1. Solar cell preparation

The solar cells analyzed in this paper were all deposited using a very simple one-stage coevaporation process. The absorber material was deposited on a soda lime glass covered with a Si(O,N) alkali diffusion barrier and a Mo back contact. The absorbers were kept ultra-thin (400nm-500nm), within a standard CIGS composition window (CGI = 0.8-0.9, GGI ~ 0.3) and had a flat Ga profile as previously discussed in [28,30,31] and shown in [3]. They were treated with alkali elements either by evaporation of thin layers of NaF before the growth of the CIGS absorber layer and/or by spincoating of KF following absorber deposition [3,30]. After absorber layer deposition and potential alkali treatment, a thin CdS buffer layer was deposited by chemical bath deposition. This is followed by sputtering of a transparent conductive oxide (TCO) consisting of a 120 nm thick intrinsic ZnO (i-ZnO) layer and a 250 nm Al-doped ZnO (AZO) layer. To contact the cells, a 50/1000/50 nm Ni/Al/Ni grid was deposited on the TCO. Devices were then isolated from each other by mechanical scribing. Each cell has an average size of 0.5 cm^2.

Some of the samples presented here have also been subjected to accelerated lifetime testing in a damp heat environment for up to 1000 hours [30].

2. Solar Cell characterization

As it was already presented by Brammertz et al. [28], our CVf data was acquired using an Agilent E4980A Precision LCR meter. The capacitance of the solar cells is measured as the DC bias voltage and the frequency of the overlaying AC voltage signal are varied. In the most simple model, changes in the measured capacitance can be linked to the capture and emission of carriers by states within the band gap of the material [17]. A change in the applied DC voltage will result in a change in space charge region width, meaning that a thicker or thinner portion of the absorber material is probed. As the frequency of the overlaying AC voltage changes, specific energy levels will respond resonantly [17]. Due to this, the frequency of the AC voltage is linked to the relative depth of the energy level. Therefore, by measuring the capacitance both as a function of bias and frequency, it is possible to obtain a 2-D parameter space that gives insight into the workings of the solar cell as a function of absorber depth as well as energy position in the band gap. In the present case, solar cells were measured at room temperature from 1kHz to 1MHz with a DC voltage bias range from -2.5V to 1V. The frequency range is covered logarithmically in 31 steps and the bias potential is gradually increased in steps of 0.1V.

By comparing the measurements obtained experimentally with simulations of specifically selected types of defects and barriers, we can then compare the resulting CVf maps and infer what effects could be at the origin of the experimentally observed responses.

The admittance simulations shown in this paper, were obtained using the SCAPS software [29]. We used a

CIGS/CdS/i-ZnO/AZO heterojunction structure similar to the one of our real solar cells. The material parameters of all the layers are the same as in our previous contribution [28,32]. To mimic our experimental measurements, the simulations in SCAPS were also performed in darkness and at 300K and assuming a series resistance of 0.5 Ωcm^2. All parameters were recorded for 31 different frequencies varying logarithmically from 1 kHz to 1 MHz and with a bias voltage ranging from -2.5 V to +1 V with a voltage step of 0.1 V.

2. EXPERIMENTAL RESULTS

When looking at the type of CVf loss maps that can be experimentally obtained during measurements on our own materials, the presence of a number of typical response domains can be noted, as presented in figure 1.

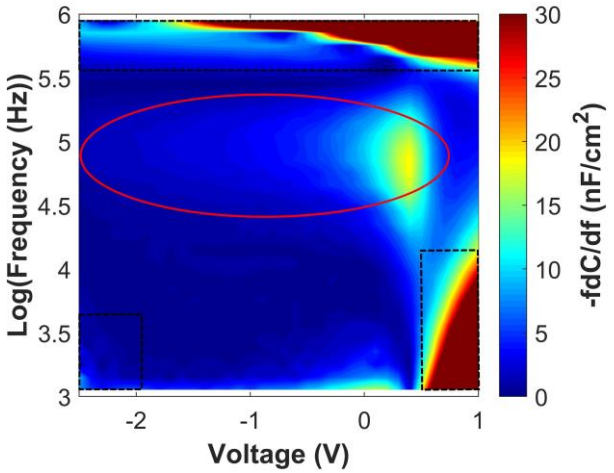

Fig. 1. Typical CVf loss map as measured experimentally. The usual response domains are highlighted using red and black contours. There is a response domain at high frequency, covering the whole bias range. The second response domain at low frequency which typically has contributions at high positive and high negative biases, symbolized by the two rectangles at low frequency. The last usual response domain is the one situation at a frequency of about 100kHz. This response domain has two major contributions, one highly intense island at positive bias and a tail-like feature that spreads out from the island and all over the bias range.

We identified three main contributions in the loss maps which can be categorized based on their position in the frequency and bias range. First, there is a pronounced response domain at the highest frequencies in our measurement window. This high frequency response domain contributes to the CVf loss map over the whole bias range. Second, a response domain can be defined at the lowest frequencies of the measurement window. This low frequency response domain has contributions that are more scattered in the bias range and are mostly visible at high positive and, occasionally, high negative biases. The last important response domain to discuss is the one located in the frequency range around 100kHz. Its main component is an intense "island" located in the forward bias and it is accompanied by a less intense "tail-like" feature that spreads all through the bias range. This contribution is highlighted in the red ellipse in figure 1.

a. Measurement related response domains

The first response domain that we identified on the CVf loss map in figure 1 is the one located at high frequency and covering most of the voltage range. In our previous work, this response domain was predicted to be caused by series resistance effects [28].

Experimentally, it is possible to verify this hypothesis by applying a slight change to the experimental setup. We did so by measuring the same solar cell using two different contact probes. The first probe is a typical two-point contact probe, whereas the second one is equipped with four contact points. By exchanging the probes used to contact the cell, we reduce the effective series resistance in the system. The comparative result of this change can be seen in figure 2.

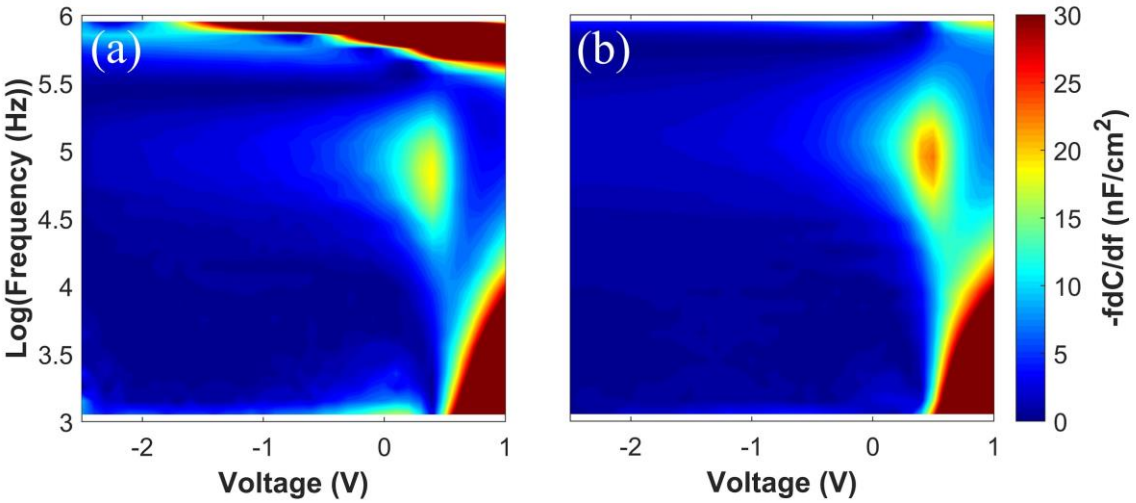

Fig. 2. CVf loss maps, as measured with a 2-point (a) and 4-point probe (b) setup. It is clearly visible that the reduction of series resistance provided by the 4-point probe setup leads to a reduction in intensity of the high frequency response domain.

As can be seen, when measuring with the four-point probe setup, the contribution of the response domain in the high frequency region is highly reduced to the point of almost disappearing completely for most of the voltage range. In the present example, figure 2(a) is the map that was measured with the two-point contact probe, which meant that the system has an effective R_s of 1.5 Ω cm^2 and figure 2(b) is measured with the four-point contact probe and has a R_s of 0.5 Ω cm^2. This result is in good agreement with the simulated effect of an increasing series resistance [28]. Therefore, this high frequency response domain can be attributed to the series resistance and will be, from now on, referred to as R_s response domain. On another note, it also becomes clear from figure 2(a) that if the series resistance of the measurement system becomes too high, the R_s response domain might interfere with other domains in the lower frequency range, as was previously discussed in [28]. This could lead to misinterpretation and mistakes during data analysis, as some important details might be hidden from view because of a very intense contribution from the series resistance. For this reason, it is important to ensure that the series resistance in the system is maintained at the lowest possible value.
The second important response domain is the one located at low frequency. In our previous contribution to the topic, we determined that this type of response domain is most likely due to dissipation, which can be defined by the following equation:

$$D = \frac{G_p}{2\pi f C_p} \ , \qquad (1)$$

where G_p and C_p are the measured values of the parallel conductance and capacitance respectively, and f is the measurement frequency. This dissipation factor D can be used to define regions of the CVf loss map in which the DC currents in the system will become too high to determine the capacitance reliably. Indeed, usual LCR meters are better equipped to measure capacitances accurately when the currents in the device are low [33]. Solar cells are, therefore, usually measured in darkness to limit noise effects due to elevated current flow. Based on the calculations we performed, we can attribute the contribution at positive bias of the low frequency domain to the dissipation. It was, moreover, suggested that this dissipation can be influenced at negative bias by shunting in the solar cell [28].

To showcase this effect, we investigated the influence of ambient light on the measurement results, and how this reflects in the CVf maps. To do so, we performed a series of measurements in which we probed cells both covered and uncovered with a dark cloth. This test was performed to generate light induced shunting and evaluate its effect on the result. This comparative measurement is presented in figure 3.

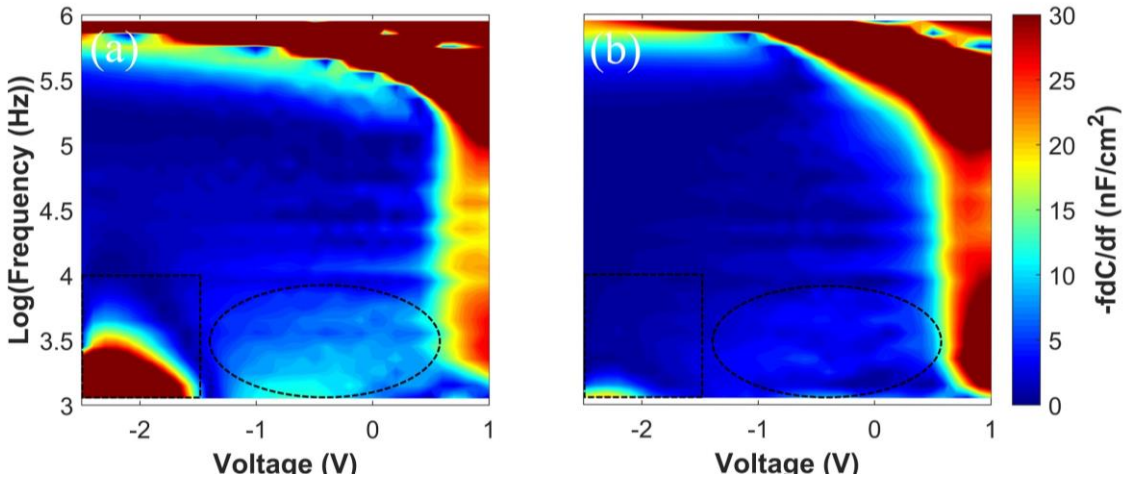

Fig. 3. CVf loss map of the same cell as measured before (a) and after (b) improving darkness conditions. The loss map in (b) shows clear improvements in measurement quality as well as the disappearance of the low frequency contribution at high negative bias.

The maps in figure 3 showcase the critical importance of keeping the cells as isolated from all light as possible. Indeed, even in the sole presence of ambient light, the resulting maps will show pronounced effects in the form of a new contribution to the low frequency response domain at high negative bias. The presence of this shunting related contribution further reduces the overall quality of the map and potentially hinders the drawing of conclusions. With this measurement, we showed that it is possible to relate both positive and negative bias contributions of the low frequency response domain. These contributions are due to high DC currents in the system and can have an additional component at high negative bias, which can be related to shunting. Due to this, we will from now on refer to the low frequency response domain as dissipation response domain.

The series resistance- and dissipation response domains we discussed so far are both related to the measurement itself. Due to this, they will always be present on most obtained CVf loss maps and can safely be disregarded from further analysis. As previously discussed, it is possible to experimentally limit the impact of the series resistance response domain by limiting the series resistance of the measurement system. When it comes to the dissipation response domain, however, it is difficult to limit its impact on the results. Shunting can be avoided by properly protecting the sample from all light sources during the measurement itself, and by selecting solar cells that have a sufficiently high R_{sh}. The dissipation contribution at high positive bias, however, is far more difficult to limit, since it is due to the presence of high DC currents, typical to that region of the bias range. This means that the absolute value of the capacitance that is measured in these regions of the map is unreliable and should not be considered during data analysis.

b. Material related response domains

At this point, most of the response domains have been analyzed and identified. The last domain that remains to be discussed is the 100kHz response domain. To identify the possible origin of this domain, we turn to simulations and identify the specific effects that can lead to a comparable behavior. To do so, we performed two sets of simulations looking at commonly expected problems for CIGS solar cells. Simulation details as well as explanatory band diagrams can be found in the supporting information.

1. Defects in the bulk CIGS material.

The first option that we need to consider is that the response at 100kHz is caused by the presence of a bulk defect since, in our previous contribution, bulk defects were already identified as the most likely candidate to be at the origin of this response domain [28]. In this case, it would explain the presence of both intensity island and tail in our CVf maps. In the most simple approach, SCAPS will simulate a bulk defect by including an additional energy level into the band gap of the bulk CIGS. This energy level is continuous over the whole bulk and has a uniform density distribution. Knowing that, it can be postulated that the tail and island of the 100kHz response domain are both the result of the same bulk defect. The island would then be the response originating from the regions closest to the CdS/CIGS interface, and the tail would be the “echo” of the same response, from deeper regions of the bulk.

To verify our hypothesis, we created an alternative problem setup in which two identical CIGS layers are used, both layers add up to the original 500nm of our absorber material, but in this simulation only the top layer, close to the CdS buffer, is affected by the bulk defect. By varying the size of the both layers, i.e. by giving more or less of the absorber to the defect free CIGS, we can vary the density profile of the bulk defect in our material and confine it to specific areas of the absorber. The simulation parameters for this simulation set can be found in table S1 of the supporting information. The results are represented in figure 4.

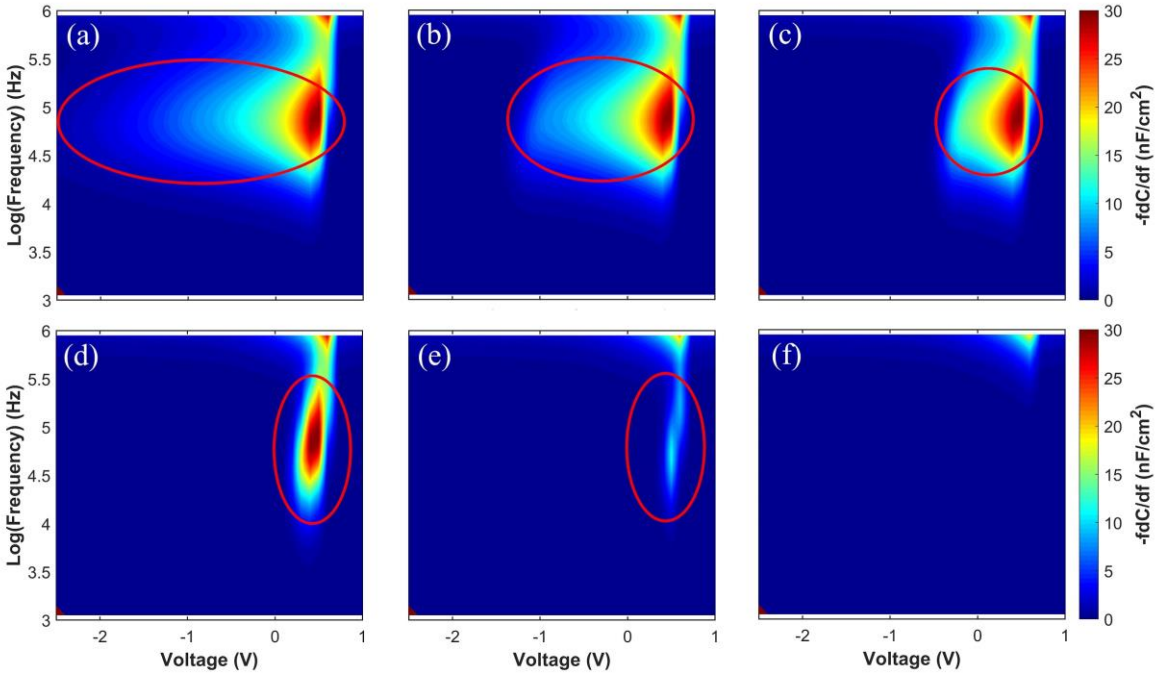

Fig. 4. Simulated CVf loss maps result of a varying thickness of a defective CIGS layer. As the thickness of the CIGS layer containing the bulk defect is reduced from 450nm (a) to 150nm (d), the tail impact of the tail in the bias range is increasingly reduced. With a 150nm thick defective layer, we are left with a situation very comparable to the impact a interface defect would have on the CVf map. If the thickness of the defective layer is reduced further down to 50nm (f) it can be seen that the defect response vanishes from the CVf map once more.

The results of this simulation set showed very clearly that, as previously postulated, the length of the tail and the thickness of the defective CIGS layer are intrinsically linked. Indeed, as the thickness of the layer containing the bulk defect was reduced from 450nm to 150nm, the impact of the tail on the bias range was greatly reduced. A 150nm thick defective layer generated a CVf response very comparable to that of an interface defect, see figure 4(d). Reducing the thickness even further, first led to the reduction in intensity of the remaining island, see figure 4(e) and the eventual complete disappearance of the response for a defective layer of 50nm, see figure 4(f).

Looking further into the topic, to verify the impact of the bulk-position of a defect energy level, we were able to achieve a similar result with a slightly different problem setup in which multiple layers of identical defect free CIGS material are separated from each other by numerical interfaces. The interface as such does not have a real impact on the simulation itself since it does not directly impact the electrical behavior of the simulated material. However, by creating additional interfaces in the absorber material, it is possible to include very local interface defect states, and thus energy levels, into them and evaluate their impact on the simulated CVf loss maps. The simulation parameters are reported in table S2 and the results of this simulation series are presented in figure 5.

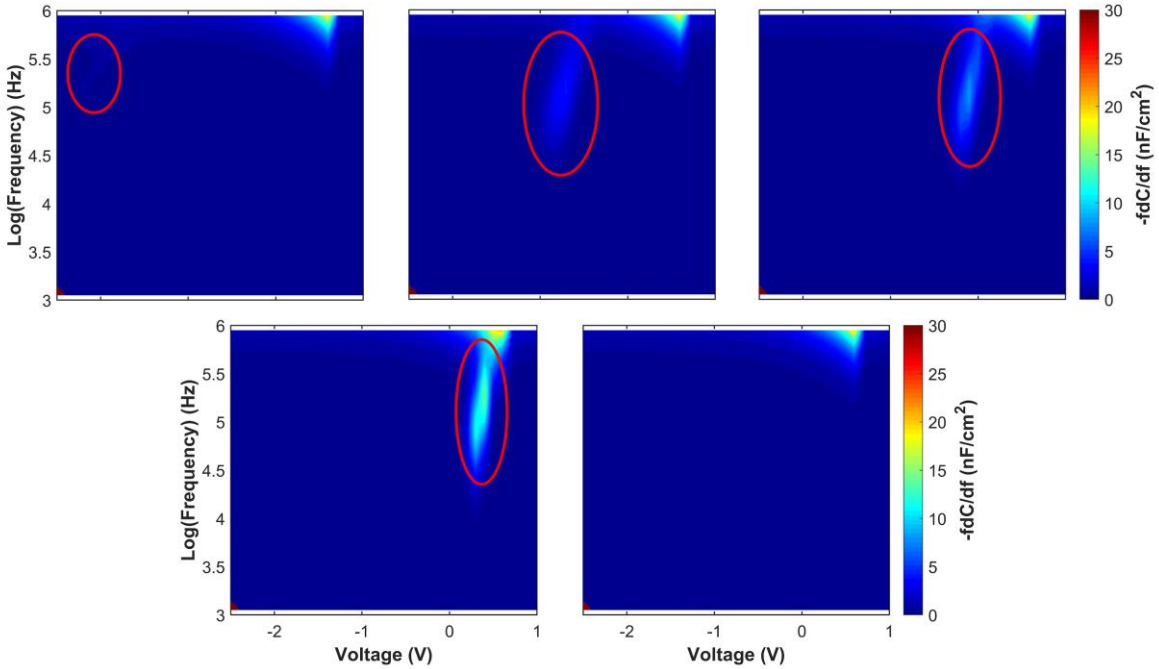

Fig. 5. Simulated CVf loss maps result of varying positions of defective interfaces. a) 450nm to f) 50nm in steps of 100nm. It can be seen that the deeper the interface is located in the absorber material, the lower the bias at which it appears on the CVf loss map. For an interface 450nm deep, the main response domain is located at about -2V, whereas for the interface located at 100nm from the CdS interface, it is located slightly above 0V. In addition to the position in bias, it can also be seen that the deeper the interface, the lower the intensity of its resulting response on the CVf loss map.

These simulations showed that the impact of the position of a defective interface in the absorber material is twofold. The deeper the interface is located in the absorber material, the lower it will be on the bias range of the resulting CVf loss map. In addition, the intensity of the response generated by the interfaces is decreasing with increasing depth. Indeed, an interface located 450nm deep into the absorber material will have CVf response domain at a bias of about -2V whereas an interface located at 100nm will be visible around 0.2V. It is also interesting to note at this point that, similar to the previous set of simulations, interfaces located 50nm off the CdS interface or closer do not appear on the CVf loss map.

Knowing that the position in the bias range and intensity of the defect island is related to the position of the interface in the absorber material, one might wonder how the CVf loss map might change if one includes multiple similar defective interfaces in the material. Indeed, given the results from the two previous simulation sets, it could be possible to obtain a CVf response similar to the one of a bulk defect, by using interface defects exclusively. To verify this, we simulated a number of defective interfaces affected by the same interface defect.
The simulation parameters are reported in table S3 and the CVf loss map resulting from this simulation is presented in figure 6.

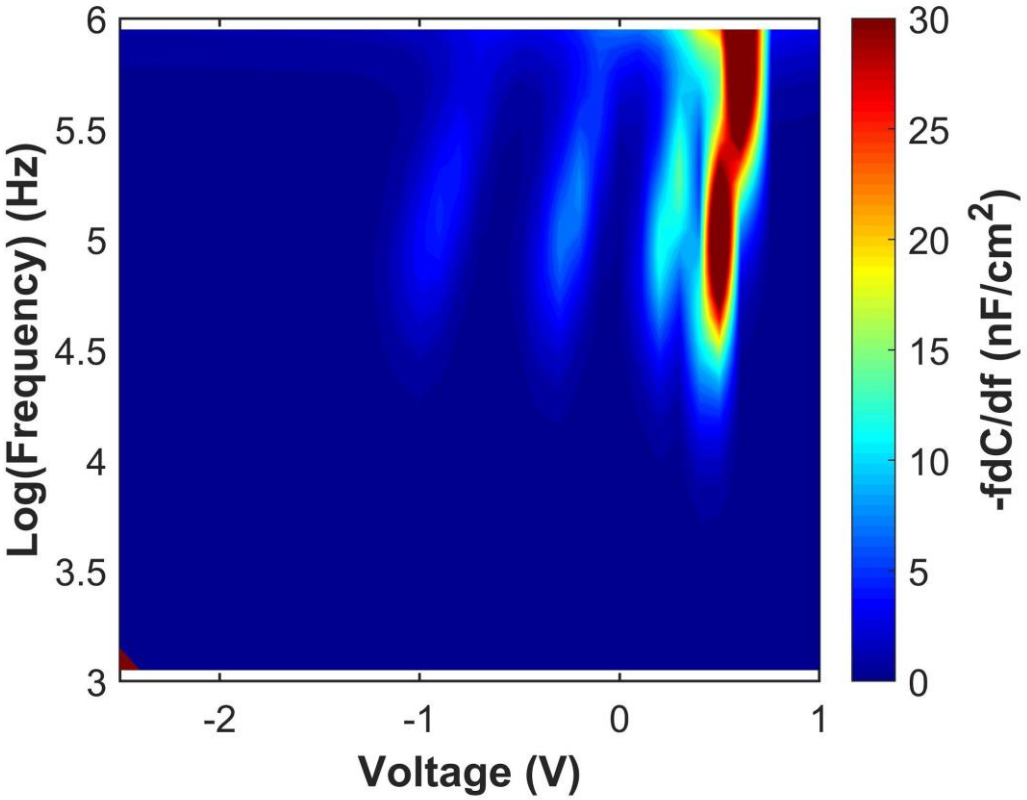

Fig. 6. Simulated CVf loss map with multiple defective interfaces. In this case, we show the effect of defects located at the CdS interface, as well as 100nm, 200nm, 300nm into the CIGS absorber material. It can be seen that the interface defect at the CdS interface is located at about 0.5V on the voltage scale and with increasing distance to the CdS interface, the defect response domain is located at lower bias. In addition, it is apparent that the further a defect is from the CdS interface, the lower its overall intensity on the CVf loss map is.

Once more, we can observe that the closer the defective interface is to the position of the CdS interface, the higher the intensity of the resulting response domain on the CVf loss map. As we move further into the CIGS absorber, the intensity islands generated by the defects slowly fade in intensity. This could explain the "fading" appearance of the tail-like feature accompanying the 100kHz response.
Unfortunately, SCAPS limits the number of layers that can be simulated, and it is, therefore, not directly possible to mimic the behavior of a bulk defect with a continuous energy level using discrete defect level positions as it was done here.
Nevertheless, the result obtained with the series of defective interfaces shows strong resemblance to the case of the bulk defect and it is reasonable to assume that given the opportunity to simulate a much larger number of interfaces, the resulting CVf map would be indiscernible from the one of the bulk defect.
These simulations clearly show that the disappearance of the tail feature of the 100kHz response domain on our CVf loss maps can be explained by applying changes to the bulk of the material. By changing the density distribution of the bulk defect, we can limit its effect to specific parts of the bias range. In this setting, the intensity island is either due to an unpassivated interface defect at the CdS/CIGS interface, as it was shown in figure 6, or it is related to the remaining effect of a bulk defect with a density distribution that is limited to a narrow region of the absorber, as was shown in figure 4(e).

2. *Problems with the CdS/CIGS interface properties.*

Based on our previous results, the second most likely explanation for the behavior of the 100kHz response domain comes from the CdS/CIGS interface. Indeed, we previously showed that conduction band offsets in this location also lead to responses that are made up an intensity island and a tail-like feature [28]. To look further into this option, we performed a number of simulations in which we artificially changed the conduction band offset (CBO) and doping at the pn junction. An example of a CVf loss map generated by such a CBO can be found in figure 7. The simulation parameters are reported in table S4.

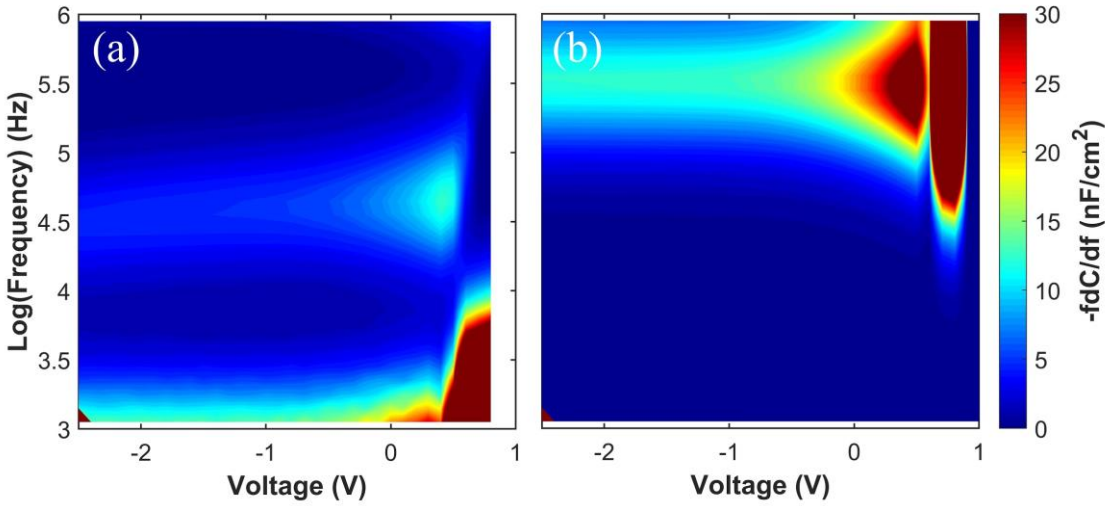

Fig. 7. Simulated CVf loss map of a CBO of 475mV (a) and 300mV (b). The intensity island of the 100kHz response domain generated by such CBOs looks similar to what was observed experimentally for the reference sample. The tail feature of the 100kHz response domain is very intense over the whole bias range and there is a very intense island.

Our simulations showed that in the same conditions as for the other simulations, visible effects of the CBO appear mostly in two ranges. First, there is a range in the vicinity of 300mV, as shown in figure 7(b). In this range, an initial response appears at the top of the CVf loss map, at high frequency. The further this band offset is increased, the further the response domain shifts into lower frequencies. Once the second window close to 475mV is reached, the initial response has almost completely left the frequency range and a second, less intense island has taken its spot in the 100kHz region. This second window of CBO has the added advantage that the remaining effects of the original response, still visible at low frequency, could be an alternative way to explain some of the low frequency domains that were previously discussed. However, if we were to extend the frequency range to lower frequencies, this original response, barely visible in the low frequencies of figure 7(a) would become fully visible again and the CVf loss map would have two separate response domains originating from the CBO. This is shown in figure S1 of the supporting information.

To date, we were unable to observe this behavior for any of our measured samples, which leads us to exclude the 475mV CBO option from further consideration as the possible origin of the 100kHz response domain in our experimental measurements. From now on, the discussed simulation results will be focussed on the 300mV CBO case.

In the case of the bulk defect, and by varying its concentration profile, we were able to isolate the origins of the island and tail of the 100kHz response domain. Thus, we performed a series of simulations to determine if the same could be done in the case of the CBO. Since in this case no defects, and thus no concentration profiles or energy levels, are involved, we looked for a different parameter to vary. For the simulations presented in figure 8, we altered the doping of the CdS, originally set to a default value of $5x10^{17}$ cm^{-3}. Detailed simulation parameters are reported in table S4.

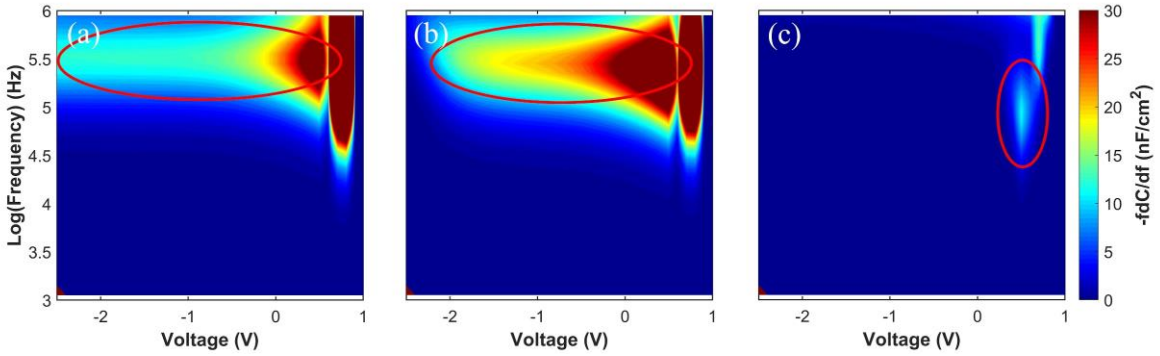

Fig. 8. Simulated CVf loss maps resulting from varying levels of CdS doping for a 300mV CBO. Represented are $5x10^{17}$ cm^{-3}(a), $3x10^{17}$ cm^{-3} (b), and $1x10^{17}$ cm^{-3}(c) .

As can be seen on figure 8, a comparatively small change to the doping of the CdS lead to a significant change in the appearance of the response domain generated by a 300mV CBO. As the doping of the CdS is lowered, the tail of the response domain disappears. For a doping of $1x10^{17}$ cm^{-3}, we are, once more, left with a response that looks very much like the response we would expect for an interface defect. Only the island of the 100kHz response remains, and the tail is completely suppressed.
The problem that remains, when considering the CBO as a possible origin for the 100kHz response domain is the high intensity of the response itself and the presence of an additional intensity island located to the right of the main response domain on the CVf loss maps. This extra domain was observed for all simulations related to the CBO but was not observed experimentally. However, given the relative simplicity of the model used here, it is very much possible that this extra response could be removed by careful calibration of the simulation parameters, carefully selecting doping levels and defects for all involved materials. In addition, it is also possible that such a response is not observed experimentally due to the interplay of the different experimental conditions. Indeed, some responses might be made visible or invisible on the experimental CVf maps due to the presence of another response or measurement artifact that would be located in the same area of the map.

c. Discussion and comparison with additional experimental results

In order to use the simulation data, presented above, to identify the exact reason for the appearance of the 100kHz domain, we analyzed two additional sets of solar cells. First, we measured and created the CVf Loss maps for a solar cell sample that was treated with KF as a post deposition treatment. The exact process that was followed for this treatment was previously described by de Wild et al. [3]. An example of the loss maps that resulted from the measurement is shown in figure 9.

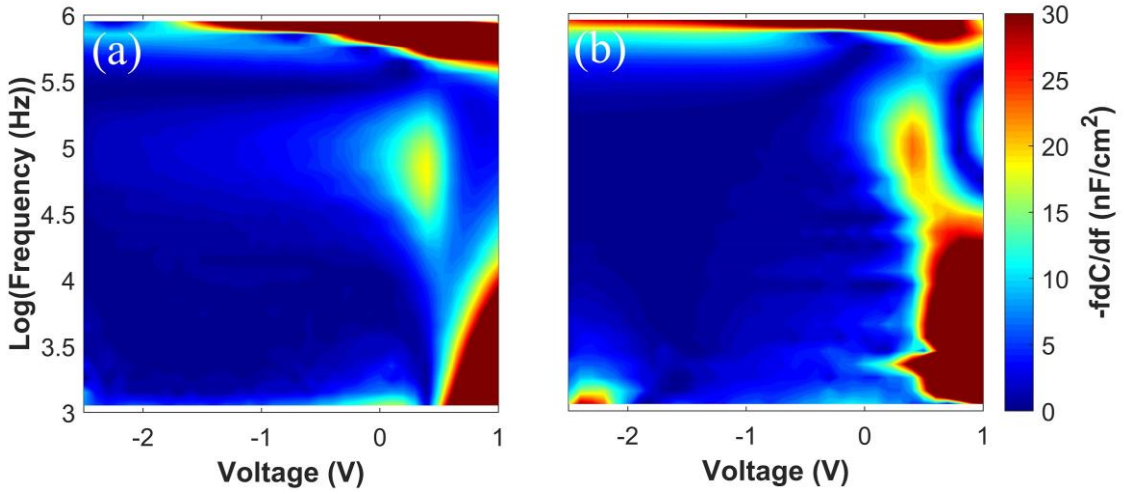

Fig. 9. The CVf loss maps as they were extracted from a measurement of a standard reference sample (a) and a cell on the KF treated sample (b). As can be seen, the tail-like feature that is typically observed in conjunction with the forward bias response domain disappears after treating the sample with potassium. The dotted line circle highlights the region of the map affected by the tail-like feature. Its absence can be noticed in (b) in the case of the potassium treated sample.

When analyzing the loss maps that are presented in figure 9, one particular detail stands out. Indeed, it appears that for the solar cell that has a KF post deposition treated absorber layer, the typical tail-like feature no longer appears on the CVf loss map. This feature was previously described as an integral part of what we defined as the 100kHz response domain. In our previous studies of the KF treated solar cells, we observed that these solar cells are significantly more efficient than their untreated counterpart [3]. This fact is now also visible on their admittance responses, since the disappearance of this tail feature on the CVf loss map means that these cells have significantly reduced electrical losses over a very wide range of biases.
Based on the previously discussed results, we can postulate at this point that, upon KF treatment, the tail of the 100kHz response domain vanished following the passivation of the bulk component of the defect at the origin of it. Indeed, we were able to link the tail to the effects of the defect in the wider bulk, whereas the island is due to effects located closer to the CdS interface. Two main explanations to this phenomenon remain and cannot truly be discarded. The first option is that we are in the case in which a bulk and interface defect of the same origin

overlap in the untreated case. After KF treatment, the bulk defect is then fully passivated, but its interface counterpart is not. The second option, presented in figure 4, is that both untreated and treated CVf maps showcase a response due to a bulk defect. In this case, the untreated cell has a bulk defect energy level that spans over the whole bulk, whereas the KF treatment limits the effect of this bulk defect to shallow regions of the absorber. This hypothesis is backed by experimental evidence of the effects of KF treatment on the bulk of the absorber, through various means [8,30,33–40].

On the other hand, KF treatment is also expected to impact the CdS/CIGS interface and more specifically the doping of the CdS [8,10,38]. This possibility was discussed in section b.2 dealing with the impact of the CBO on the CVf loss maps. These simulations showed that even a minimal reduction in the CdS doping could potentially lead to a total disappearance of the tail associated with the conduction band offset.

To investigate the matter further, we performed CVf measurements on a similar set of samples that were treated with KF before being exposed to accelerated lifetime testing in damp heat conditions [30]. Bias dependent admittance measurements were taken at regular intervals all through the degradation process and the resulting maps are presented in figure 10.

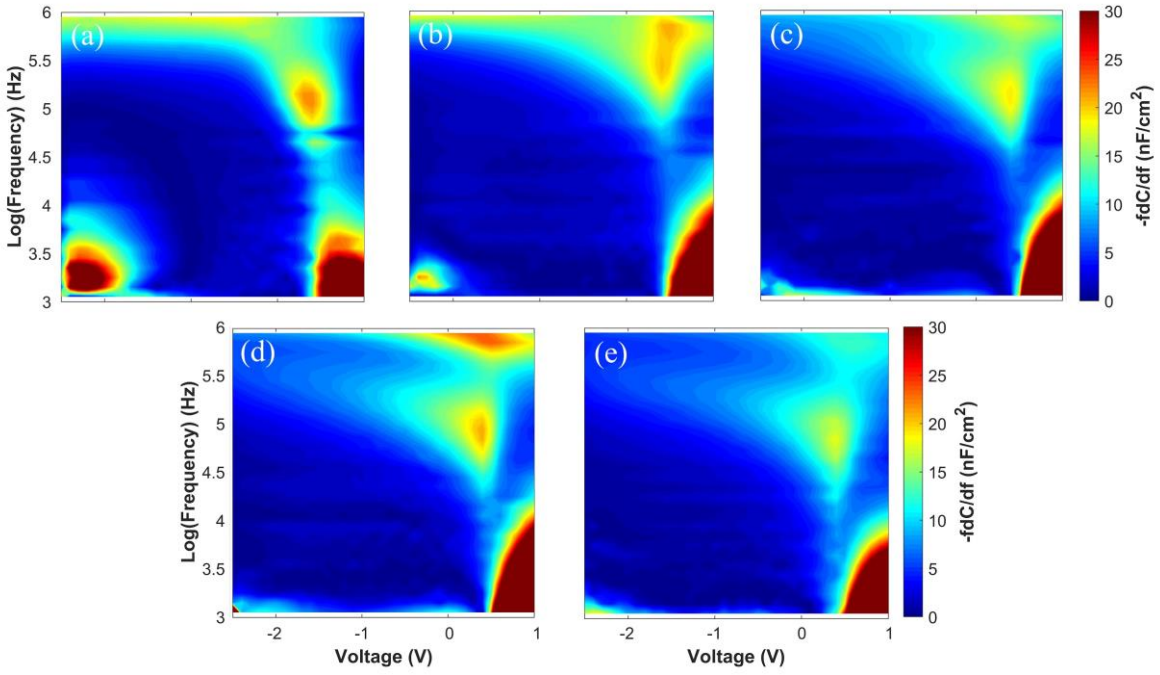

Fig. 10. Evolution of the measured CVf loss maps as the sample is exposed to damp heat for extended periods of time. The timesteps represented here are, (a) 0h (Unaged), (b) 250h, (c) 500h, (d) 750h, and (e) 1000h of damp heat treatment. This particular sample was treated with KF and does, therefore not present the usual tail-like feature of the forward bias response domain at first. As it degrades in the aggressive and water rich environment, however, the tail-like feature reappears and intensifies as the degradation process progresses.

Looking at the loss maps in figure 10, it becomes clear that, as time goes on, the tail feature of the forward bias response domain gradually reappears and intensifies as the degradation of the damp heat exposed sample progresses. At 0 hours and 250h of exposure, the cell does not showcase a tail-like feature for the 100kHz response domain. The feature becomes visible again after 500 hours of exposure to moisture and is fully formed for 750 hours and 1000 hours. It also appears that with increasing exposure time, the response observed response domain slightly shifts in the frequency range.

Once more, both hypotheses developed in the previous parts of this contribution could be plausible explanations for the effects we observed in the case of the samples submitted to accelerated lifetime testing. On the one hand, the extended exposure to heat and humidity could affect the buffer layer and change its properties.

On the other hand, for the solar cells exposed to a damp heat environment, we were able to show that water occupies the grain boundaries of single stage coevaporated CIGS during their extended stay in an environment with high room humidity and temperature [30]. Based on this observation, the grain boundaries can be identified as a possible common origin for the effects observed in both cases presented above. Indeed, it has also been reported before that potassium and other heavy alkali have a tendency to occupy the grain boundaries and change their properties [8,30,33–40]. Knowing this, it is very possible that the tail feature that we observe in our CVf loss maps could be a contribution linked to the presence of grain boundaries in our material. This effect could be

further exacerbated by the fact that, being one-stage coevaporated CIGS, the grains in our material are on average very small and, thus, the absorber layer showcases a high concentration of grain boundaries for the K atoms to passivate [30]. This would mean that in our accelerated lifetime experiment, originally, the grain boundaries are passivated by the presence of K. They are, subsequently, in their current state, not detrimental to the workings of the solar cell and do not appear on the CVf loss map. As the degradation time increases, an increasing amount of water seeps into the grain boundaries of the absorber, which, in turn, leads to the gradual reappearance and intensification of the tail-like feature on the CVf loss map.

If, as we just exposed, we consider the grain boundaries to be responsible for the tail feature in our experimental CVf maps, we can perform one more simulation to try and determine what happens in the grain boundary when we apply the KF treatment. Indeed, one common hypothesis is that the grain boundaries in CIGS are mostly benign because of the band offset that is generated in this particular region of the material [8]. To verify this, we can define a limited defective region in our CIGS absorber, representing a grain boundary, and simulate its impact on the CVf loss map before and after we apply a band offset to it. The simulation parameters and resulting band diagrams are reported in figure S3 and table S5 while the results of this set of simulations are presented in figure 11.

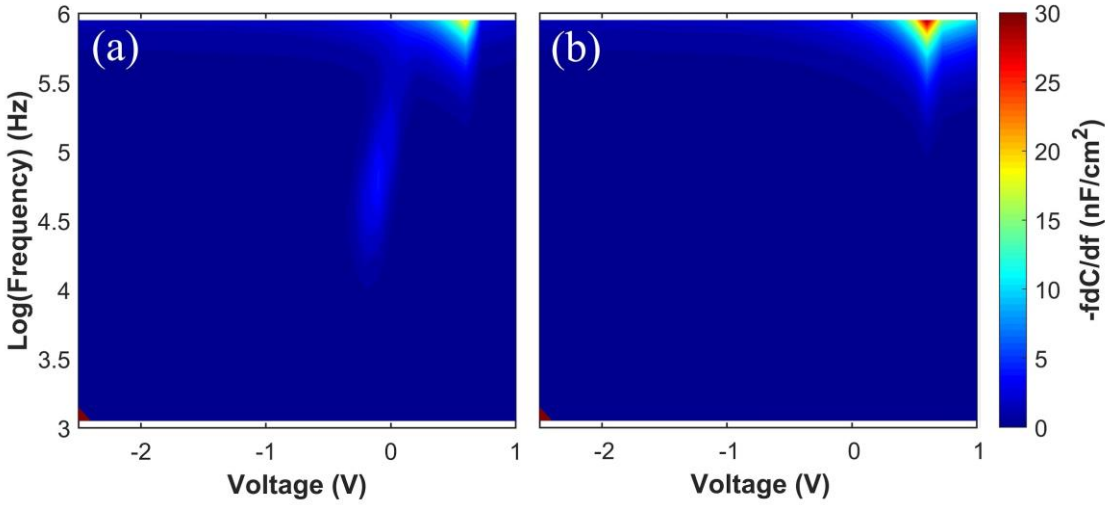

Fig. 11. The CVf loss maps as they were simulated for a defective 10nm thick grain boundary layer with (a) and without (b) 200mV band offset [8]. It can be seen that in the presence of a band offset, the CVf response of the defective layer disappears from the visible range on the CVf map.

When we perform this simulation, it becomes apparent that if we apply a 200mV band offset [8] to the grain boundary layer, the previously visible CVf response, vanishes from the map by shifting out of the visible range. With the water seeping into the grain boundaries of the bulk during accelerated lifetime, we would then observe the effect of progressively reducing this band offset, shifting the response back into the visible range on the CVf map.

This result further confirms that our model with the grain boundaries at the origin of the observed 100kHz response domain is plausible.

However, using this type of simulation trick only allows for the simulation of interfaces that are horizontally positioned in the absorber material, i.e. parallel to the Mo and CdS of interfaces. Interfaces that run vertically from the back contact to the CdS interface cannot be simulated this way. It cannot be excluded that these vertical grain boundaries would play a role in the electrical behavior of the solar cell as well but it is generally accepted that horizontal interfaces are much more likely to be detrimental to the performance of CIGS, given that they are obstacles that carriers need to overcome to be effectively extracted for current [41].

Even though the conduction band offset cannot be fully excluded, we believe that the configuration of defects, presented in figure 6, could more accurately explain the experimentally measured behavior of our samples. In this case, a defect close to the CdS interface would be the main defect responsible for the high intensity island of the 100kHz response domain, whereas a more or less continuous series of defective interfaces or layers all through the absorber material would be responsible for the accompanying tail-like feature.

3. CONCLUSIONS

Using the experimental measurements exposed in this paper, we were able to confirm several of the effects that our previous simulations predicted. In particular, we were able to link a response domain at very high frequency to the series resistance. Indeed, by using a four point contact probe to perform the measurement, rather than the version with two contact points, it was possible to greatly reduce the series resistance in the measurement system, and subsequently, limit the intensity and presence of this contribution to the CVf loss map. Another set of response domains, located at the lowest frequencies in our measurement window, could be identified as an impact of dissipation, similar to what was predicted by previous calculations [28]. In relation to the previous observation, we also showed what influence ambient light has on the CVf loss map and outlined the importance of proper light isolation of the measurement system. Both of the response domains discussed above are related to the measurement itself and their impact on the overall result can only be limited rather than entirely avoided.

The second, novel, part of our investigation was focused on trying to identify the origin of the other recurring artifact, the 100kHz response domain. This response domain was described as a combination of two contributions. First, the response domain itself, which is a high intensity island on the CVf map in the forward bias. Second, the tail-like feature that accompanies this high intensity island. This contribution of much lower intensity was observed to be located in the same frequency range as the high intensity island and spread all over the bias range. By measuring solar cells that underwent a potassium fluoride post deposition treatment and subsequent artificial ageing in a damp heat environment, we were able to infer that the origin of this tail-like feature is either related to the grain boundaries in the bulk of the absorber material, or the band offset at the CdS/CIGS interface. Indeed, following the potassium treatment of the absorber, we were able to observe its disappearance. This disappearance could be explained using SCAPS simulations in which we assumed changing density distributions for bulk defects or changes to the doping of the CdS buffer layer. As the samples were artificially aged and the solar cell was exposed to water, the tail of the 100kHz response domain progressively reappeared. This could be due to the fact that water is seeping into the grain boundaries of the absorber material, subsequently changing their properties. On the other hand, progressive oxidation of the CdS, leading to an increase in its band gap and a resulting increase in CBO at the CdS/CIGS interface, is also a plausible explanation. Even if the tail disappeared and reappeared with the above described treatments the high intensity spot-like feature it is related to remained visible on the CVf loss map at all times. Therefore, we concluded that the experimentally observed loss maps are likely due to the effects of a combination of different types of bulk and interface defects or interface barriers with adequate energy positions in the band gap. The identification of the exact phenomenon at the origin of this domain is, however, still complicated. Indeed, CIGS solar cells are a highly complex combination of layers and interfaces, each one of which comes with a plethora of defects and barriers. All these potentially have similar effects on the overall appearance of the 100kHz response domain, based both on their respective energies and carrier capture cross-sections. Nevertheless, the results presented in this contribution have highlighted the power and possible range of application of this novel way of representing bias dependent admittance spectroscopy in the form of CVf loss map. This approach could be used to study a wide variety of cases and investigate the impact of different process steps. In a first step, this can be applied to CIGS solar cells, to observe and demonstrate the presence of different types of defects and barriers in the solar cell. Eventually, this approach could be applied to other types of solar cells or electrical devices as well, and the reasons limiting the performance of the currently available materials and device architectures could be investigated further.

ACKNOWLEDGEMENTS

The work published in this paper was supported by the European Research Council (ERC) under the Union's Horizon 2020 research and innovation program (grant agreement No 715027).

REFERENCES

[1] M.A. Green, E.D. Dunlop, J. Hohl-Ebinger, M. Yoshita, N. Kopidakis, A.W.Y. Ho-Baillie, Solar cell efficiency tables (Version 55), Prog. Photovoltaics Res. Appl. 28 (2020) 3–15. https://doi.org/10.1002/pip.3228.

[2] J. de Wild, M. Simor, D.G. Buldu, T. Kohl, G. Brammertz, M. Meuris, J. Poortmans, B. Vermang, Alkali treatment for single-stage co-evaporated thin CuIn0.7Ga0.3Se2 solar cells, Thin Solid Films. 617 (2019) 44–48. https://doi.org/https://doi.org/10.1016/j.tsf.2018.12.022.

[3] J. de Wild, D.G. Buldu, T. Schnabel, M. Simor, T. Kohl, G. Birant, G. Brammertz, M. Meuris, J. Poortmans, B. Vermang, High V oc upon KF Post-Deposition Treatment for Ultrathin Single-Stage Coevaporated Cu(In, Ga)Se 2 Solar Cells, ACS Appl. Energy Mater. 2 (2019) 6102–6111. https://doi.org/10.1021/acsaem.9b01370.

[4] E. Avancini, R. Carron, T.P. Weiss, C. Andres, M. Bürki, C. Schreiner, R. Figi, Y.E. Romanyuk, S. Buecheler, A.N. Tiwari, Effects of Rubidium Fluoride and Potassium Fluoride Postdeposition Treatments on Cu(In,Ga)Se2

Thin Films and Solar Cell Performance, Chem. Mater. 29 (2017) 9695–9704. https://doi.org/10.1021/acs.chemmater.7b03412.
[5] R. Carron, S. Nishiwaki, T. Feurer, R. Hertwig, E. Avancini, J. Löckinger, S.C. Yang, S. Buecheler, A.N. Tiwari, Advanced Alkali Treatments for High-Efficiency Cu(In,Ga)Se2 Solar Cells on Flexible Substrates, Adv. Energy Mater. 9 (2019) 1–8. https://doi.org/10.1002/aenm.201900408.
[6] A. Chirilă, P. Reinhard, F. Pianezzi, P. Bloesch, A.R. Uhl, C. Fella, L. Kranz, D. Keller, C. Gretener, H. Hagendorfer, D. Jaeger, R. Erni, S. Nishiwaki, S. Buecheler, A.N. Tiwari, Potassium-induced surface modification of Cu(In,Ga)Se2 thin films for high-efficiency solar cells, Nat. Mater. 12 (2013) 1107–1111. https://doi.org/10.1038/nmat3789.
[7] P. Jackson, R. Wuerz, D. Hariskos, E. Lotter, W. Witte, M. Powalla, Effects of heavy alkali elements in Cu(In,Ga)Se2 solar cells with efficiencies up to 22.6%, Phys. Status Solidi - Rapid Res. Lett. 10 (2016) 583–586. https://doi.org/10.1002/pssr.201600199.
[8] S. Siebentritt, E. Avancini, M. Bär, J. Bombsch, E. Bourgeois, S. Buecheler, R. Carron, C. Castro, S. Duguay, R. Félix, E. Handick, D. Hariskos, V. Havu, P. Jackson, H.P. Komsa, T. Kunze, M. Malitckaya, R. Menozzi, M. Nesladek, N. Nicoara, M. Puska, M. Raghuwanshi, P. Pareige, S. Sadewasser, G. Sozzi, A.N. Tiwari, S. Ueda, A. Vilalta-Clemente, T.P. Weiss, F. Werner, R.G. Wilks, W. Witte, M.H. Wolter, Heavy Alkali Treatment of Cu(In,Ga)Se2 Solar Cells: Surface versus Bulk Effects, Adv. Energy Mater. 10 (2020). https://doi.org/10.1002/aenm.201903752.
[9] Y. Sun, S. Lin, W. Li, S. Cheng, Y. Zhang, Y. Liu, W. Liu, Review on Alkali Element Doping in Cu(In,Ga)Se2 Thin Films and Solar Cells, Engineering. 3 (2017) 452–459. https://doi.org/10.1016/J.ENG.2017.04.020.
[10] M. Rusu, T. Kodalle, L. Choubrac, N. Barreau, C.A. Kaufmann, R. Schlatmann, T. Unold, Electronic Structure of the CdS/Cu(In,Ga)Se 2 Interface of KF- and RbF-Treated Samples by Kelvin Probe and Photoelectron Yield Spectroscopy , ACS Appl. Mater. Interfaces. (2021). https://doi.org/10.1021/acsami.0c20976.
[11] C. Hubert, N. Naghavi, O. Roussel, A. Etchberry, D. Harikos, R. Menner, M. Pozalla, O. Kerrec, D. Lincot, The Zn(S,O,OH)/ZnMgO Buffer in Solar Cells Part I: Fast Chemical Thin Film Cu(In,Ga)(S,Se)2-Based Bath Deposition of Zn(S,O,OH) Buffer Layers for Industrial Application on Co-evaporated CuIn(S,Se)2 Solar Cells Cu(In,Ga)Se2 and Electrodeposited, Prog. Photovoltaics Res. Appl. 17 (2009) 470–478. https://doi.org/10.1002/pip898.
[12] A. Ennaoui, M. Bär, J. Klaer, K. T., R. Sáez-Araoz, M.C. Lux-Steiner, Highly-efficient Cd-free CuInS2 Thin-film Solar Cells and Mini-modules with Zn(S,O) Buffer Layers Prepared by an Alternative Chemical Bath Process, Prog. Photovoltaics Res. Appl. 14 (2006) 499–511. https://doi.org/10.1002/pip682.
[13] M. Buffière, S. Harel, L. Arzel, C. Deudon, N. Barreau, J. Kessler, Fast chemical bath deposition of Zn(O,S) buffer layers for Cu(In,Ga)Se 2 solar cells, Thin Solid Films. 519 (2011) 7575–7578. https://doi.org/10.1016/j.tsf.2011.01.104.
[14] X. Lin, H. Li, F. Qu, H. Gu, W. Wang, Cu(In,Ga)Se2 solar cell with Zn(S,O) as the buffer layer fabricated by a chemical bath deposition method, Sol. Energy. 171 (2018) 130–141. https://doi.org/10.1016/j.solener.2018.06.070.
[15] E.H. Nicollian, J.R. Brews, MOS (Metal Oxide Semiconductor) Physics and Technology, Wiley, 2002. https://www.wiley.com/en-fi/MOS+%28Metal+Oxide+Semiconductor%29+Physics+and+Technology-p-9780471430797.
[16] T. Walter, R. Herberholz, C. Müller, H.W. Schock, Determination of defect distributions from admittance measurements and application to Cu (In , Ga) Se2 based heterojunctions Determination of defect distributions from admittance measurements and application to Cu (In , Ga) Se 2 based heterojunctions, J. Appl. Phys. 80 (1996) 4411–4419. https://doi.org/10.1063/1.363401.
[17] D. Abou-ras, T. Kirchartz, U. Rau, Advanced Characterization Techniques for Thin Film Solar CThomasells, Wiley-VCH Verlag GmbH, 2011. https://doi.org/10.1002/9783527636280.
[18] M. Burgelman, P. Nollet, Admittance spectroscopy of thin film solar cells, Solid State Ionics. 176 (2005) 2171–2175. https://doi.org/10.1016/j.ssi.2004.08.048.
[19] F. Werner, S. Siebentritt, Buffer Layers, Defects, and the Capacitance Step in the Admittance Spectrum of a Thin-Film Solar Cell, Phys. Rev. Appl. 9 (2018) 54047. https://doi.org/10.1103/PhysRevApplied.9.054047.
[20] J. Bailey, G. Zapalac, D. Poplavskyy, Metastable defect measurement from capacitance-voltage and admittance measurements in Cu(In, Ga)Se2 Solar Cells, Conf. Rec. IEEE Photovolt. Spec. Conf. 2016–Novem (2016) 2135–2140. https://doi.org/10.1109/PVSC.2016.7750011.
[21] J.M.V. Cunha, C. Rocha, C. Vinhais, P.A. Fernandes, P.M.P. Salome, Understanding the AC Equivalent Circuit Response of Ultrathin Cu(In,Ga)Se2 Solar Cells, IEEE J. Photovoltaics. 9 (2019) 1442–1448. https://doi.org/10.1109/JPHOTOV.2019.2927918.
[22] G. Brammertz, S. Oueslati, M. Buffière, J. Bekaert, H. Elanzeery, K.B. Messaoud, S. Sahayaraj, T. Nuytten, C. Köble, M. Meuris, J. Poortmans, Investigation of Properties Limiting Efficiency in Cu2ZnSnSe4-Based Solar Cells, IEEE J. Photovoltaics. 5 (2014) 649–655. https://doi.org/10.1109/JPHOTOV.2014.2376053.
[23] S. Oueslati, G. Brammertz, M. Buffière, H. Elanzeery, O. Touayar, C. Köble, J. Bekaert, M. Meuris, J. Poortmans, Physical and electrical characterization of high-performance Cu2ZnSnSe4 based thin film solar cells, Thin Solid Films. 582 (2015) 224–228. https://doi.org/10.1016/j.tsf.2014.10.052.
[24] R. Herberholz, M. Igalson, H.W. Schock, Distinction between bulk and interface states in spectroscopy Distinction between bulk and interface states in CuInSe 2 / CdS / ZnO by space charge spectroscopy, J. Appl. Phys. 83 (1997) 318–325. https://doi.org/10.1063/1.366686.
[25] K. Decock, S. Khelifi, S. Buecheler, F. Pianezzi, A.N. Tiwari, M. Burgelman, Defect distributions in thin film solar cells deduced from admittance measurements under different bias voltages, J. Appl. Phys. 110 (2011) 063722. https://doi.org/10.1063/1.3641987.

[26] T. Eisenbarth, T. Unold, R. Caballero, C.A. Kaufmann, H.W. Schock, Interpretation of admittance, capacitance-voltage, and current-voltage signatures in Cu(In,Ga)Se2thin film solar cells, J. Appl. Phys. 107 (2010) 034509. https://doi.org/10.1063/1.3277043.
[27] T. Eisenbarth, R. Caballero, M. Nichterwitz, C.A. Kaufmann, H.W. Schock, T. Unold, Characterization of metastabilities in Cu(In,Ga)Se2 thin-film solar cells by capacitance and current-voltage spectroscopy, J. Appl. Phys. 110 (2011) 094506. https://doi.org/10.1063/1.3656453.
[28] G. Brammertz, T. Kohl, J. de Wild, D.G. Buldu, G. Birant, M. Meuris, J. Poortmans, B. Vermang, Bias-Dependent Admittance Spectroscopy of Thin-Film Solar Cells: Experiment and Simulation, IEEE J. Photovoltaics. 10 (2020) 1102–1111. https://doi.org/10.1109/JPHOTOV.2020.2992350.
[29] M. Burgelman, P. Nollet, S. Degrave, Modelling polycrystalline semiconductor solar cells, Thin Solid Films. 361 (2000) 527–532. https://doi.org/10.1016/S0040-6090(99)00825-1.
[30] T. Kohl, N.A. Rivas, J. de Wild, D.G. Buldu, G. Birant, G. Brammertz, M. Meuris, F.U. Renner, J. Poortmans, B. Vermang, Inclusion of Water in Cu(In, Ga)Se 2 Absorber Material During Accelerated Lifetime Testing, ACS Appl. Energy Mater. 3 (2020) 5120–5125. https://doi.org/10.1021/acsaem.0c00610.
[31] D.G. Buldu, J. de Wild, T. Kohl, S. Suresh, G. Birant, G. Brammertz, M. Meuris, J. Poortmans, B. Vermang, Wet processing in state-of-the-art cu(In,ga)se2 thin film solar cells, Solid State Phenom. 282 SSP (2018) 300–305. https://doi.org/10.4028/www.scientific.net/SSP.282.300.
[32] C. Frisk, C. Platzer-Björkman, J. Olsson, P. Szaniawski, J.T. Wätjen, V. Fjällström, P. Salomé, M. Edoff, Optimizing Ga-profiles for highly efficient Cu(In, Ga)Se2 thin film solar cells in simple and complex defect models, J. Phys. D. Appl. Phys. 47 (2014) 485104. https://doi.org/10.1088/0022-3727/47/48/485104.
[33] A. Stokes, M. Al-Jassim, D. DIercks, A. Clarke, B. Gorman, Impact of Wide-Ranging Nanoscale Chemistry on Band Structure at Cu(In, Ga)Se2 Grain Boundaries, Sci. Rep. 7 (2017) 1–11. https://doi.org/10.1038/s41598-017-14215-0.
[34] A. Vilalta-Clemente, M. Raghuwanshi, S. Duguay, C. Castro, E. Cadel, P. Pareige, P. Jackson, R. Wuerz, D. Hariskos, W. Witte, Rubidium distribution at atomic scale in high efficient Cu(In,Ga)Se2 thin-film solar cells, Appl. Phys. Lett. 112 (2018) 103105. https://doi.org/10.1063/1.5020805.
[35] P. Schöppe, S. Schönherr, P. Jackson, R. Wuerz, W. Wisniewski, M. Ritzer, M. Zapf, A. Johannes, C.S. Schnohr, C. Ronning, Overall Distribution of Rubidium in Highly Efficient Cu(In,Ga)Se2 Solar Cells, ACS Appl. Mater. Interfaces. 10 (2018) 40592–40598. https://doi.org/10.1021/acsami.8b16040.
[36] F. Pianezzi, P. Reinhard, A. Chirilă, B. Bissig, S. Nishiwaki, S. Buecheler, A.N. Tiwari, Unveiling the effects of post-deposition treatment with different alkaline elements on the electronic properties of CIGS thin film solar cells, Phys. Chem. Chem. Phys. 16 (2014) 8843–8851. https://doi.org/10.1039/c4cp00614c.
[37] N. Nicoara, R. Manaligod, P. Jackson, D. Hariskos, W. Witte, G. Sozzi, R. Menozzi, S. Sadewasser, Direct evidence for grain boundary passivation in Cu(In,Ga)Se2 solar cells through alkali-fluoride post-deposition treatments, Nat. Commun. 10 (2019) 1–8. https://doi.org/10.1038/s41467-019-11996-y.
[38] C.P. Muzzillo, J.D. Poplawsky, H.M. Tong, W. Guo, T. Anderson, Revealing the beneficial role of K in grain interiors, grain boundaries, and at the buffer interface for highly efficient CuInSe2 solar cells, Prog. Photovoltaics Res. Appl. 26 (2018) 825–834. https://doi.org/10.1002/pip.3022.
[39] M. Raghuwanshi, E. Cadel, S. Duguay, L. Arzel, N. Barreau, P. Pareige, Influence of Na on grain boundary and properties of Cu(In,Ga)Se2 solar cells, Prog. Photovoltaics Res. Appl. 25 (2017) 367–375. https://doi.org/10.1002/pip.2869.
[40] M. Raghuwanshi, A. Vilalta-Clemente, C. Castro, S. Duguay, E. Cadel, P. Jackson, D. Hariskos, W. Witte, P. Pareige, Influence of RbF post deposition treatment on heterojunction and grain boundaries in high efficient (21.1%) Cu(In,Ga)Se 2 solar cells, Nano Energy. 60 (2019) 103–110. https://doi.org/10.1016/j.nanoen.2019.03.028.
[41] U. Rau, K. Taretto, S. Siebentritt, Grain boundaries in Cu(In,∈Ga)(Se,∈S)2 thin-film solar cells, Appl. Phys. A Mater. Sci. Process. 96 (2009) 221–234. https://doi.org/10.1007/s00339-008-4978-0.